Multicolor Photometry of Tiny Near-Earth Asteroid 2015 RN$_{35}$ across a Wide Range of Phase Angles: Possible Mission-accessible A-type Asteroid

Jin Beniyama[1,2], Ryou Ohsawa[3], Chrysa Avdellidou[4], Shigeyuki Sako[1,5,6], Satoshi Takita[1], Masateru Ishiguro[7,8], Tomohiko Sekiguchi[9], Fumihiko Usui[10], Shinichi W. Kinoshita[2,3], Kianhong Lee[1,3,11], Asami Takumi[3,12], Marin Ferrais[13], and Emmanuël Jehin[14]

[1] Institute of Astronomy, Graduate School of Science, The University of Tokyo, 2-21-1 Osawa, Mitaka, Tokyo 181-0015, Japan; beniyama@ioa.s.u-tokyo.ac.jp
[2] Department of Astronomy, Graduate School of Science, The University of Tokyo, 7-3-1 Hongo, Bunkyo-ku, Tokyo 113-0033, Japan
[3] National Astronomical Observatory of Japan, 2-21-1 Osawa, Mitaka, Tokyo 181-8588, Japan
[4] Université Côte d'Azur, Observatoire de la Côte d'Azur, CNRS, Laboratoire Lagrange, Bd de l'Observatoire, CS 34229, F-06304 Nice Cedex 4, France
[5] UTokyo Organization for Planetary Space Science, The University of Tokyo, 7-3-1 Hongo, Bunkyo-ku, Tokyo 113-0033, Japan
[6] Collaborative Research Organization for Space Science and Technology, The University of Tokyo, 7-3-1 Hongo, Bunkyo-ku, Tokyo 113-0033, Japan
[7] Department of Physics and Astronomy, Seoul National University, 1 Gwanak-ro, Gwanak-gu, Seoul 08826, Republic of Korea
[8] SNU Astronomy Research Center, Seoul National University, 1 Gwanak-ro, Gwanak-gu, Seoul 08826, Republic of Korea
[9] Asahikawa Campus, Hokkaido University of Education, Hokumon 9, Asahikawa, Hokkaido 070-8621, Japan
[10] Institute of Space and Astronautical Science, Japan Aerospace Exploration Agency, 3-1-1 Yoshinodai, Chuo-ku, Sagamihara, Kanagawa 252-5210, Japan
[11] Astronomical Institute, Tohoku University, Sendai 980-8578, Japan
[12] Open University of Japan, 2-11 Wakaba, Mihama-ku, Chiba 261-8586, Japan
[13] Arecibo Observatory, University of Central Florida, HC-3 Box 53995, Arecibo, PR 00612, USA
[14] Space sciences, Technologies and Astrophysics Research (STAR) Institute, Université de Liège, Allée du 6 Août 17, B-4000 Liège, Belgium

Abstract

Studying small near-Earth asteroids is important in order to understand their dynamical histories and origins as well as to mitigate the damage caused by asteroid impacts on Earth. We report the results of multicolor photometry of the tiny near-Earth asteroid 2015 RN$_{35}$ using the 3.8 m Seimei telescope in Japan and the TRAPPIST-South telescope in Chile over 17 nights in 2022 December and 2023 January. We observed 2015 RN$_{35}$ across a wide range of phase angles from $2°$ to $30°$ in the g, r, i, and z bands in the Pan-STARRS system. These lightcurves show that 2015 RN$_{35}$ is in a nonprincipal axis spin state with two characteristic periods of 1149.7 ± 0.3 s and 896.01 ± 0.01 s. We found that the slope of the visible spectrum of 2015 RN$_{35}$ is as red as asteroid (269) Justitia, one of the very red objects in the main belt, which indicates that 2015 RN$_{35}$ can be classified as an A- or Z-type asteroid. In conjunction with the shallow slope of the phase curve, we suppose that 2015 RN$_{35}$ is a high-albedo A-type asteroid. We demonstrated that surface properties of tiny asteroids could be well constrained by intensive observations across a wide range of phase angles. 2015 RN$_{35}$ is a possible mission-accessible A-type near-Earth asteroid with a small Δv of $11.801 \mathrm{~km~s}^{-1}$ in the launch window between 2030 and 2035.

Unified Astronomy Thesaurus concepts: Asteroids (72); Near-Earth objects (1092); Photometry (1234); Multicolor photometry (1077); Light curves (918)

1. Introduction

It is now well established that the first stage of the process of planetary formation is the accretion of so-called planetesimals from the solids in our protoplanetary disk. Theoretical and observational studies have shown that planetesimals were formed at large sizes, with diameters (D) larger than 50–100 km (Delbo et al. 2017). The small bodies of our solar system are remnants of that era. However, not all the current asteroids are survivors from primordial times. Collisions among this original planetesimal population produced clusters of fragments of smaller sizes, the so-called asteroid families. A nongravitational effect—the Yarkovsky effect—slowly changes the orbital semimajor axis a of asteroids at a rate da/dt proportional to $1/D$ (Vokrouhlický 1998). Asteroids in prograde rotation have $da/dt > 0$ and migrate toward larger heliocentric distances, whereas those in retrograde rotation with $da/dt < 0$ migrate toward the Sun. Another effect that is also

caused by the solar radiation, the Yarkovsky–O'Keefe–Radzievskii–Paddack (YORP) effect (Rubincam 2000), can change the spin state of asteroids and affect the rate of drift due to the Yarkovsky effect. Both the Yarkovsky and YORP effects depend on the surface properties of the asteroids and their internal structure. The migration of small main belt asteroids (MBAs) can lead the smaller ones to reach the dynamical routes (resonances with planets) that can bring them to near-Earth space, hence sampling several regions (as well as asteroid families) of the main belt. Studying near-Earth asteroids (NEAs) is therefore crucial in order to understand the transport of material from the main belt to near-Earth space as well as to mitigate the hazard of an asteroid impact on Earth.

Tiny asteroids having diameters less than 100 m could be characterized during their close approaches to the Earth using ground-based and space-borne telescopes. Comprehensive studies of large asteroids have been conducted, whereas few studies focus on tiny asteroids due to observational difficulties caused by their limited visibility and large apparent motions during such close approaches.

Using the Infrared Array Camera (IRAC) on the Spitzer Space Telescope, Mommert et al. (2014a, 2014b) conducted infrared observations of the tiny NEAs 2009 BD ($D \leqslant 5$ m) and

2011 MD ($D \sim 10$ m). According to these observations, asteroid 2009 BD has an inconclusive surface nature and could be either covered by fine regolith or composed of a collection of bare rocks, while the bulk density of 2011 MD is estimated to be $1.1^{+0.7}_{-0.5} \times 10^3$ kg m^{-3}, indicating a rubble-pile origin. Recently, Fenucci et al. (2021, 2023) found that the tiny superfast rotators (499998) 2011 PT ($D \sim 35$ m and rotation period $P \sim 10$ minutes) and 2016 GE$_1$ ($D \sim 12$ m and $P \sim 34$ s) have small thermal conductivities of $K \leqslant 0.1$ W m^{-1} K^{-1} and $K \leqslant 100$ W m^{-1} K^{-1}, respectively. Such small conductivities imply that these two tiny asteroids are covered with fine regolith or highly porous rocks (Avdellidou et al. 2020; Cambioni et al. 2021). On the other hand, a number of fast rotators have been discovered in video observations using a CMOS camera (Beniyama et al. 2022). Some of them need to have strength similar to the typical tensile strength of meteorites to keep their fast rotations. It is unclear whether such a fast rotator could have fine regolith on its surface. Thus, it is still in debate whether tiny asteroids are monolithic or rubble-pile, and with or without fine regolith on their surface.

Reddy et al. (2016) conducted radar, lightcurve, and spectroscopic observations of the tiny E-type NEA 2015 TC$_{25}$ ($D \sim 2$ m). They concluded that 2015 TC$_{25}$ is a fragment possibly ejected from the E-type main belt asteroid (44) Nysa. One of the interesting properties of 2015 TC$_{25}$ is its bluer spectrum compared to a typical E-type. They explained the bluer slope of 2015 TC$_{25}$ in the visible wavelengths with a lack of fine regolith on the surface due to a combination of weak gravity and fast rotation. Recently, Licandro et al. (2023) found that a visible spectrum of the tiny fast-rotating asteroid 2022 AB ($D \sim 65$ m and $P \sim 3$ minutes) shows an upturn over the range 0.4–0.6 μm, which does not fit with any known asteroid spectrum.[15]

The phase-angle dependence of an asteroid's brightness, the so-called phase curve, informs about the surface properties of the asteroid (see, e.g., Bowell et al. 1989; Belskaya & Shevchenko 2000). High-albedo asteroids have a shallower slope in their phase curves since the contribution of shadow-hiding decreases as albedo increases (Belskaya & Shevchenko 2000), whereas low-albedo asteroids have steeper slopes. Apart from the albedo, other properties are related to the phase curve such as the surface grain size and roughness. An important consideration in studying phase curves of asteroids is the rotation correction (see, e.g., Harris & Lupishko 1989). Homogeneous sets of the typical brightness such as maximum and mean of the lightcurves at certain phase angles are necessary to accurately derive the related quantities, otherwise the brightness variation caused by rotation leads to misunderstanding of observational results. Thus, the tiny asteroids, which are often fast-rotating (Thirouin et al. 2016, 2018; Beniyama et al. 2022) and do not require a long time to obtain a mean brightness across a rotation phase, are appropriate targets for investigating phase curves.

Well-sampled phase curves of small asteroids are less commonly obtained since opportunities for their observation are limited. Reddy et al. (2015) characterized the small NEA 2004 BL$_{86}$ ($D \sim 300$ m) over a wide phase-angle range from 1°.5 to 49°.6. The visible geometric albedo of about 0.4 derived from the slope of the phase curve is consistent with the near-infrared spectrum of 2004 BL$_{86}$, which implies that 2004 BL$_{86}$

is a typical high-albedo V-type asteroid. Recently, several dozen phase curves of NEAs have been studied in the framework of the IMPACTON project (Rondón et al. 2019, 2022; Ieva et al. 2022; Arcoverde et al. 2023). This project created a database with phase curves of 30 NEAs using three 1 m class telescopes in Brazil and Italy (Arcoverde et al. 2023). Their sample includes only one tiny NEA, 2017 DC$_{38}$, with an absolute magnitude H of 24.22, which was successfully observed at a very small phase angle of 1°.1. However, its rotation period was not obtained and thus no rotation correction has been performed in the analysis of its phase curve.

In this paper, we present the results of multicolor photometry of the tiny NEA 2015 RN$_{35}$ over 17 nights in Japan and Chile. The target asteroid 2015 RN$_{35}$ was discovered by the Pan-STARRS 1 survey (Chambers et al. 2016) on 2015 September 9. 2015 RN$_{35}$ is an Apollo-class NEA, and its absolute magnitude in the V band is 23.24 in the NASA JPL Small-Body Database (SBDB).[16] The trajectories of 2015 RN$_{35}$ were well studied and possible collisions with Earth were discussed (Petrov et al. 2018). 2015 RN$_{35}$ had a close approach in 2022 December: it was observable at phase angles from 30° to 0°.6 from 2022 December to 2023 January, which is a quite rare opportunity to obtain a well-sampled phase curve of a tiny asteroid. The paper is organized as follows. In Section 2, we summarize our observations and data reduction. The physical properties of 2015 RN$_{35}$ are summarized in Section 3. The surface properties of the tiny asteroid 2015 RN$_{35}$ and possible exploration by a spacecraft mission are discussed in Section 4.

2. Observations and Data Reduction

We conducted photometric observations at two observatories in Japan and Chile. The observing conditions are summarized in Table 1. The predicted V-band magnitudes, phase angles, distances between 2015 RN$_{35}$ and observer, and distances between 2015 RN$_{35}$ and the Sun in Table 1 were obtained from NASA JPL HORIZONS[17] using the `Python` package `astroquery` (Ginsburg et al. 2019).

2.1. Seimei Telescope

We obtained 12 lightcurves of 2015 RN$_{35}$ using the TriColor CMOS Camera and Spectrograph (TriCCS) on the 3.8 m Seimei telescope (Kurita et al. 2020) from 2022 December 23 to 2023 January 21. We simultaneously took three-band images in the Pan-STARRS (g, r, i) and (g, r, z) filters (Chambers et al. 2016). The field of view is 12′.6 × 7′.5 with a pixel scale of 0″.350 pixel^{-1}.

Nonsidereal tracking was performed during the observations of 2015 RN$_{35}$. The exposure times were 5 or 60 s according to the brightness of 2015 RN$_{35}$. The signal-to-noise ratios of 2015 RN$_{35}$ in the data taken in 2023 January are too low to detect 2015 RN$_{35}$ in a single exposure. We took multiple images with short exposures rather than a single image with long exposures in our observations in order to avoid having elongated photometric reference stars and also to eliminate cosmic rays.

We performed standard image reduction including bias subtraction, dark subtraction, and flat-fielding. The astrometry of reference sources from the Gaia Data Release 2 was performed using the `astrometry.net` software (Lang et al. 2010). For

---

[15] We note that the spectrum is similar to that of the Martian Trojan (121514) 1998 UJ$_7$ (Borisov et al. 2018).

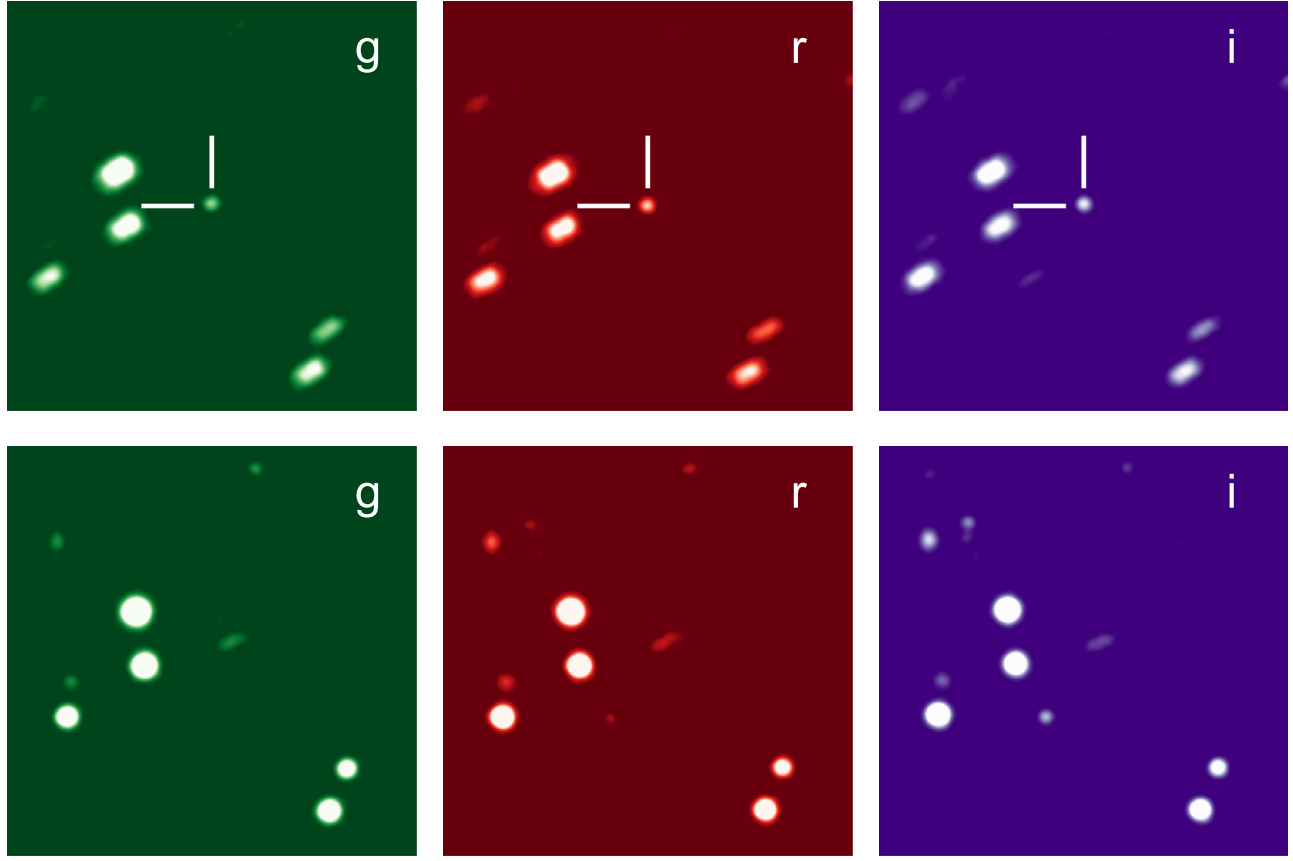[16] https://ssd.jpl.nasa.gov/tools/sbdb_lookup.html, last accessed 2023 August 10.
[17] https://ssd.jpl.nasa.gov/horizons

Figure 1. Stacked images of 2015 RN$_{35}$ in g, r, and i bands with a total integration time of 1200 s in 2023 January 16. Nonsidereally stacked images (top) and sidereally stacked images (bottom) are shown. Horizontal and vertical bars indicate 2015 RN$_{35}$. The field of view covers $1\rlap{.}'75 \times 1\rlap{.}'75$. North is to the top and east is to the left.

Table 1
Summary of the Observations

Obs. Date (UTC)	Telescope	Filter	t_{exp} (s)	N_{img}	V (mag)	α (deg)	Δ (au)	r_{h} (au)	Air Mass	Weather
2022 Dec 19 05:05:40–08:40:18	TRAPPIST-S	*Exo*	40	233	15.3	31.1	0.014	0.996	1.24–1.48	Clear
2022 Dec 20 02:46:27–04:00:16	TRAPPIST-S	*Exo*	40	83	15.7	31.3	0.017	0.998	1.71–2.64	Clear
2022 Dec 21 07:13:33–08:34:49	TRAPPIST-S	*Exo*	40	91	16.1	31.1	0.021	1.002	1.32–1.51	Clear
2022 Dec 22 06:02:40–08:40:00	TRAPPIST-S	*Exo*	40	171	16.5	30.7	0.024	1.004	1.33–1.55	Clear
2022 Dec 23 16:32:56–17:14:41	Seimei	*g, r, i*	5	394	16.8	30.0	0.029	1.008	1.07–1.09	Clear
2022 Dec 23 19:03:49–19:45:32	Seimei	*g, r, z*	5	275	16.9	29.9	0.029	1.009	1.20–1.33	Clear
2022 Dec 26 05:04:08–08:39:14	TRAPPIST-S	*Exo*	120	100	17.4	28.1	0.037	1.016	1.39–1.64	Clear
2022 Dec 26 18:09:43–18:35:49	Seimei	*g, r, i*	30	53	17.5	27.7	0.039	1.018	1.10–1.14	Clear
2023 Jan 12 12:15:06–12:35:09	Seimei	*g, r, i*	1200	2	19.1	10.9	0.100	1.082	1.52–1.66	Cirrus
2023 Jan 16 14:54:23	Seimei	*g, r, i*	1200	1	19.3	6.7	0.117	1.100	1.06–1.06	Clear
2023 Jan 17 12:11:24	Seimei	*g, r, i*	1200	1	19.3	5.8	0.121	1.104	1.53–1.53	Cirrus
2023 Jan 18 14:07:50–14:30:15	Seimei	*g, r, i*	1200	2	19.4	4.7	0.125	1.109	1.08–1.11	Clear
2023 Jan 18 14:51:09	Seimei	*g, r, z*	1200	1	19.4	4.7	0.126	1.109	1.06–1.06	Clear
2023 Jan 20 14:04:41	Seimei	*g, r, i*	1200	1	19.4	2.8	0.134	1.118	1.10–1.10	Clear
2023 Jan 20 14:25:34	Seimei	*g, r, z*	1200	1	19.4	2.8	0.134	1.118	1.07–1.07	Clear
2023 Jan 21 14:03:12	Seimei	*g, r, i*	1200	1	19.4	1.9	0.139	1.123	1.10–1.10	Clear
2023 Jan 21 14:27:02–14:47:05	Seimei	*g, r, z*	1200	2	19.4	1.9	0.139	1.123	1.05–1.07	Clear

Note. Observation time in UT at midtime of exposure (Obs. Date), telescope, filters, total exposure time per frame (t_{exp}), number of images (N_{img}), and weather conditions are listed. Predicted V-band apparent magnitude (V), phase angle (α), distance between 2015 RN$_{35}$ and observer (Δ), and distance between 2015 RN$_{35}$ and Sun (r_{h}) at the observation starting time are referred to NASA Jet Propulsion Laboratory (JPL) HORIZONS as of 2023 August 19 (UTC). Elevations of 2015 RN$_{35}$ to calculate air mass range are also referred to NASA JPL HORIZONS.

the data taken in 2023 January, we performed stacking of images before photometry to avoid elongations of the images of 2015 RN$_{35}$ as shown in the upper panels of Figure 1 (hereinafter referred to as the nonsidereally stacked image). We stacked 20 successive images with exposure times of 60 s. Since a typical readout time of the CMOS sensors on TriCCS is 0.4 ms, the total

integration time is about 1200 s, which corresponds to one of the characteristic periods of 2015 RN$_{35}$ (see Section 3.1). We also stacked images using the World Coordinate System (WCS) of images corrected with the surrounding sources to suppress the elongations of the images of reference stars as shown in the lower panels of Figure 1 (hereinafter referred to as the sidereally stacked image).

We derived colors and magnitudes of 2015 RN$_{35}$ following the procedure described in Beniyama et al. (2023a, 2023b). Cosmic rays were removed with the Python package astroscrappy (McCully et al. 2018) using Pieter van Dokkum's L.A.Cosmic algorithm (van Dokkum 2001). Circular aperture photometry was performed for 2015 RN$_{35}$ and the reference stars using the SExtractor-based Python package sep (Bertin & Arnouts 1996; Barbary et al. 2017). The aperture radii were set to be twice as large as the FWHMs of the point-spread functions of the reference stars in the sidereally stacked images. The photometric results of 2015 RN$_{35}$ and reference stars were obtained from the nonsidereally and sidereally stacked images, respectively.

2.2. TRAPPIST-South Telescope

We obtained five lightcurves of 2015 RN$_{35}$ using the robotic telescope TRAPPIST-South (the Minor Planet Center code I40; Jehin et al. 2011) of the University of Liège between 2022 December 19 and 26. TRAPPIST-South is a 0.6 m Ritchey–Chrétien telescope operating at $f/8$ and equipped with a CCD camera FLI ProLine 3041-BB. The field of view is $22' \times 22'$ with an unbinned pixel scale of $0\rlap{.}''64$ pixel^{-1}.

We obtained images in the sidereal tracking mode with the wide Exo filter, whose wavelength coverage roughly corresponds to the r to y bands in the Pan-STARRS system (Jehin et al. 2011). We set exposure time to 40 s on December 19, 20, 21, and 22 using the 2×2 binning mode, and to 120 s on December 26 while using no binning.

The raw images were processed using standard bias, dark, and flat-field frames. The photometry was performed using the PHOTOMETRYPIPELINE (Mommert 2017) to derive the r-band magnitudes in the Pan-STARRS system. This pipeline allows zero-point calibration by matching field stars with online catalogs. Typically 100 stars with solar-like colors (i.e., stars with $g - r$ and $r - i$ colors closer than 0.2 mag to that of the Sun) were used in each image for the magnitude calibration. Aperture radii were set to 4 pixels for the binned observations and to 8 pixels for the unbinned mode.

3. Results

3.1. Lightcurves and Rotation Period

The light-travel time was corrected to obtain the time-series colors and magnitudes of 2015 RN$_{35}$ (Harris & Lupishko 1989). The eight lightcurves of 2015 RN$_{35}$ taken on 2022 December are shown in Figure 2. Brightness variation of about 0.7 mag is seen in each lightcurve. The lightcurves show imperfect periodic signals, implying that 2015 RN$_{35}$ is a nonprincipal axis rotator in a complex rotation state (i.e., a tumbler; Pravec et al. 2005).

We performed the periodic analysis using the Lomb–Scargle technique (Lomb 1976; Scargle 1982; VanderPlas 2018) with three long lightcurves obtained with the TRAPPIST-South telescope on 2022 December 19, 22, and 26. The Lomb–Scargle periodograms with a range of period from 500 to

2000 s are shown in Figure 3, where four peak frequencies, f_a, f_b, f_c, and f_d, are indicated. We focused on the two strongest frequencies, f_b and f_d, based on the powers of periodograms. f_d appears to be the first overtone of f_b: $2f_b \fallingdotseq f_d$. We considered that f_b corresponds to a period of 2015 RN$_{35}$, P_1, since folded lightcurves with f_b^{-1} are typical double-peaked lightcurves. The uncertainty of P_1 was estimated with the Monte Carlo technique following the previous work (Beniyama et al. 2022). We obtained 1000 lightcurves by randomly resampling the data assuming each observed data point follows a normal distribution whose standard deviation is a photometric error. We calculated the 1000 periods corresponding to P_1 and derived it with the uncertainty each night as 1149.7 ± 0.4 s (December 19), 1149.6 ± 0.5 s (December 22), and 1149.9 ± 0.5 s (December 26). We adopted the error-weighted average of these three periods, 1149.7 ± 0.3, as P_1.

Figure 4 shows the eight r-band lightcurves of 2015 RN$_{35}$ folded with a period of 1149.7 s. The folded lightcurves seem to be double-peaked but do not perfectly overlap each other in rotation phase, probably due to the nonprincipal axis rotation. The model curve with the period of 1149.7 s is also shown in Figure 4. The rms of the residual is calculated as follows:

$$\mathrm{RMS} = \sqrt{\sum_{i}^{n_{\mathrm{obs}}} \frac{[y_{\mathrm{obs}}(t_i) - y_{\mathrm{model}}(t_i)]^2}{n_{\mathrm{obs}}}} \tag{1}$$

where n_{obs} is the number of observation data, t_i is the observation time of the ith sample, $y_{\mathrm{obs}}(t_i)$ is the ith observed brightness at t_i, and $y_{\mathrm{model}}(t_i)$ is the model brightness at t_i. The rms is calculated as 0.104.

Franco et al. (2023) derived the rotation period of 2015 RN$_{35}$ to be 0.3193 ± 0.0001 hr ~ 1149 s using lightcurves obtained on 2022 December 18 and 19. Koleńczuk et al. (2023) found a rotation period of 19.1692 ± 0.0069 minutes ~ 1150 s from an intensive observation campaign during 2022 December. These reported periods are close to P_1 and correspond to f_b in Figure 3. On the other hand, Colazo et al. (2023) derived the rotation period of 2015 RN$_{35}$ to be 0.478 ± 0.008 hr ~ 1721 s using lightcurves obtained on 2022 December 16, which corresponds to f_a in Figure 3. Since the phased lightcurves in Colazo et al. (2023) appear as not double-peaked unlike others, the rotation period of ~ 1150 is highly likely.

We continue the periodic analysis for the three lightcurves obtained with the TRAPPIST-South telescope on 2022 December 19, 22, and 26 following procedures in previous studies (Pravec et al. 2005, 2014; Lee et al. 2017, 2022). The purpose of successive analysis is to derive the other period P_2 characterizing the nonprincipal axis rotation of 2015 RN$_{35}$. Searching for P_2 is performed against all five lightcurves obtained with the TRAPPIST-South telescope. We fit the lightcurves with two-dimensional Fourier series keeping P_1 fixed:

$$
\begin{aligned}
y_{\mathrm{model}}(t) = C_0 &+ \sum_{j=1}^{m} \left[C_{j0} \cos\left(\frac{2\pi j}{P_1} t\right) + S_{j0} \sin\left(\frac{2\pi j}{P_1} t\right) \right] \\
&+ \sum_{k=1}^{m} \sum_{j=-m}^{m} \left[C_{jk} \cos\left(\frac{2\pi j}{P_1} t + \frac{2\pi k}{P_2} t\right) \right. \\
&\left. + S_{jk} \sin\left(\frac{2\pi j}{P_1} t + \frac{2\pi k}{P_2} t\right) \right],
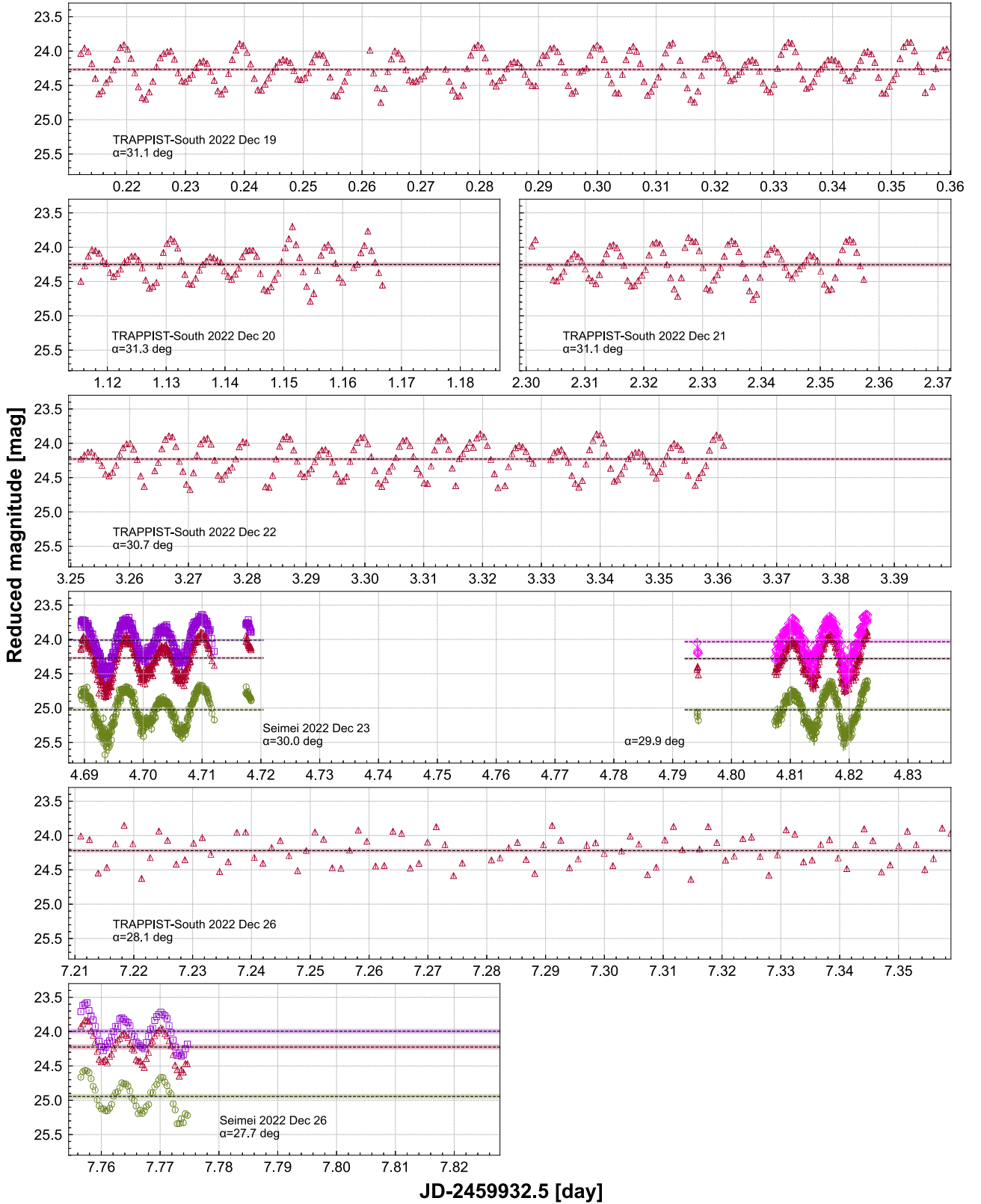\end{aligned}
\tag{2}
$$

Figure 2. Lightcurves of 2015 RN$_{35}$. The reduced g-, r-, i-, and z-band magnitudes are presented as circles, triangles, squares, and diamonds, respectively. Bars indicate the 1σ uncertainties. The error-weighted average of magnitude in each lightcurve is presented with a dashed line. Shaded areas indicate the standard errors of the weighted averaged magnitudes.

where t is time, m is the order of Fourier series, and C_0, C_{jk}, and S_{jk} are the Fourier coefficients. We set P_2 and the Fourier coefficients as free parameters and searched for P_2 from 100 s

to 10,000 s with a step of 1 s. The rms residual between observed and model lightcurves of 2015 RN$_{35}$ is calculated in each step. The results of the search for P_2 are shown in

5
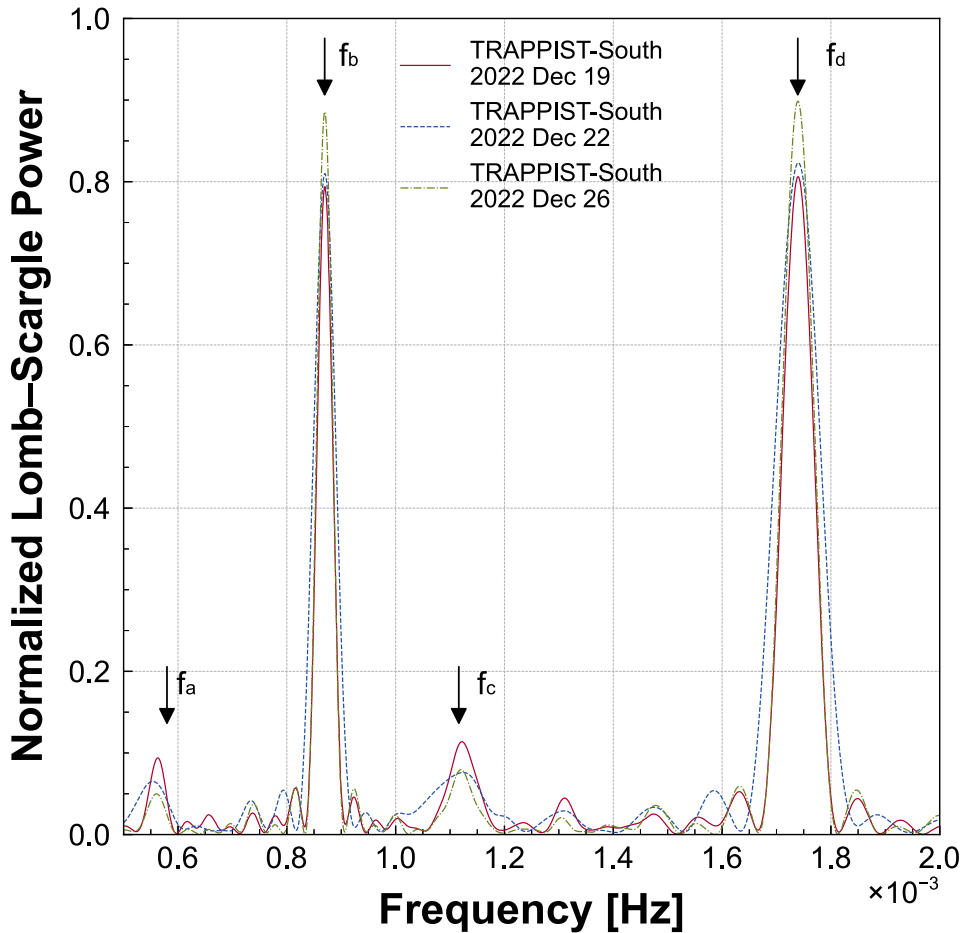
Figure 3. Lomb–Scargle periodogram of 2015 RN$_{35}$. The number of harmonics is two. The three periodograms were created using lightcurves obtained with the TRAPPIST-South telescope on 2022 December 19, 22, and 26. Four peak frequencies in each case are indicated.

Figure 5. We plotted the results of a grid search for P_2 in cases with m of 3 and 4. Five periods with smaller rms in the two cases, $P_a = 896$ s, $P_b = 1603$ s, $P_c = 2688$ s, $P_d = 4062$ s, and $P_e = 8123$ s, are indicated in Figure 5. The five periods might be linear combinations of the two basic periods. These appear to be related to each other: $P_b^{-1} \fallingdotseq P_c^{-1} + P_d^{-1}$, $P_c = 3P_a$, $2P_d \fallingdotseq 9P_a$, and $P_e \fallingdotseq 2P_d$. Thus, we regard the shortest period P_a as P_2, which is a period independent of P_1. This P_2 corresponds to the third strongest peak, f_c, in Figure 3. We also estimated the uncertainty of P_2 with the Monte Carlo technique like that of P_1. We derived P_2 as 896.01 ± 0.01 s with 1000 randomly resampled lightcurves.

The model curves with P_1 of 1149.7 s and P_2 of 896.01 s are shown in Figure 6 with the observed lightcurves. The rms is calculated as 0.069. The model and observed lightcurves overlap each other well, which indicates that P_1 and P_2 are periods characterizing the rotation state of 2015 RN$_{35}$. We note that P_1 and P_2 may not necessarily correspond to rotation and precession (or precession and rotation) periods, respectively. Determination of the rotation and precession periods needs detailed physical modeling, which is out of the scope of this paper.

3.2. Colors and Reflectance Spectrum

The time series of colors of 2015 RN$_{35}$ in 2022 December are shown in Figure 7. The error-weighted averages of those colors are derived as $g - r = 0.714 \pm 0.008$, $r - i = 0.245 \pm 0.009$, and $r - z = 0.255 \pm 0.020$. The systematic errors in color determination with TriCCS are considered as in Beniyama et al. (2023b). The error-weighted average colors correspond to each other within the measurement errors when we consider the results in 2023 January (see Figure 9(b)).

The reflectance spectrum of 2015 RN$_{35}$ in Figure 8 was calculated with the derived colors and the solar colors using the method in Beniyama et al. (2023a). The reflectances at the central wavelength of the r, i, and z bands, R_r, R_i, and R_z, were calculated as

$$R_r = 10^{-0.4[(r-g)_{\mathrm{RN}_{35}} - (r-g)_\odot]}, \qquad (3)$$

$$R_i = 10^{-0.4[(i-g)_{\mathrm{RN}_{35}} - (i-g)_\odot]}, \qquad (4)$$

$$R_z = 10^{-0.4[(z-g)_{\mathrm{RN}_{35}} - (z-g)_\odot]}, \qquad (5)$$

where $(r - g)_{\mathrm{RN}_{35}}$, $(i - g)_{\mathrm{RN}_{35}}$, and $(z - g)_{\mathrm{RN}_{35}}$ are the colors of 2015 RN$_{35}$, whereas $(r - g)_\odot$, $(i - g)_\odot$, and $(z - g)_\odot$ are the colors of the Sun in the Pan-STARRS system. We referred to the absolute magnitude of the Sun in the Pan-STARRS system as $g = 5.03$, $r = 4.64$, $i = 4.52$, and $z = 4.51$ (Willmer 2018). We set the uncertainties of the magnitudes of the Sun as 0.02.

The reflectance spectra in Figure 8 are normalized at the center of the g band in the Pan-STARRS system, 0.481 μm (Tonry et al. 2012). The horizontal bars in 2015 RN$_{35}$'s spectrum indicate the filter bandwidths. The reflectance spectra apart from 2015 RN$_{35}$ were originally normalized at 0.55 μm.
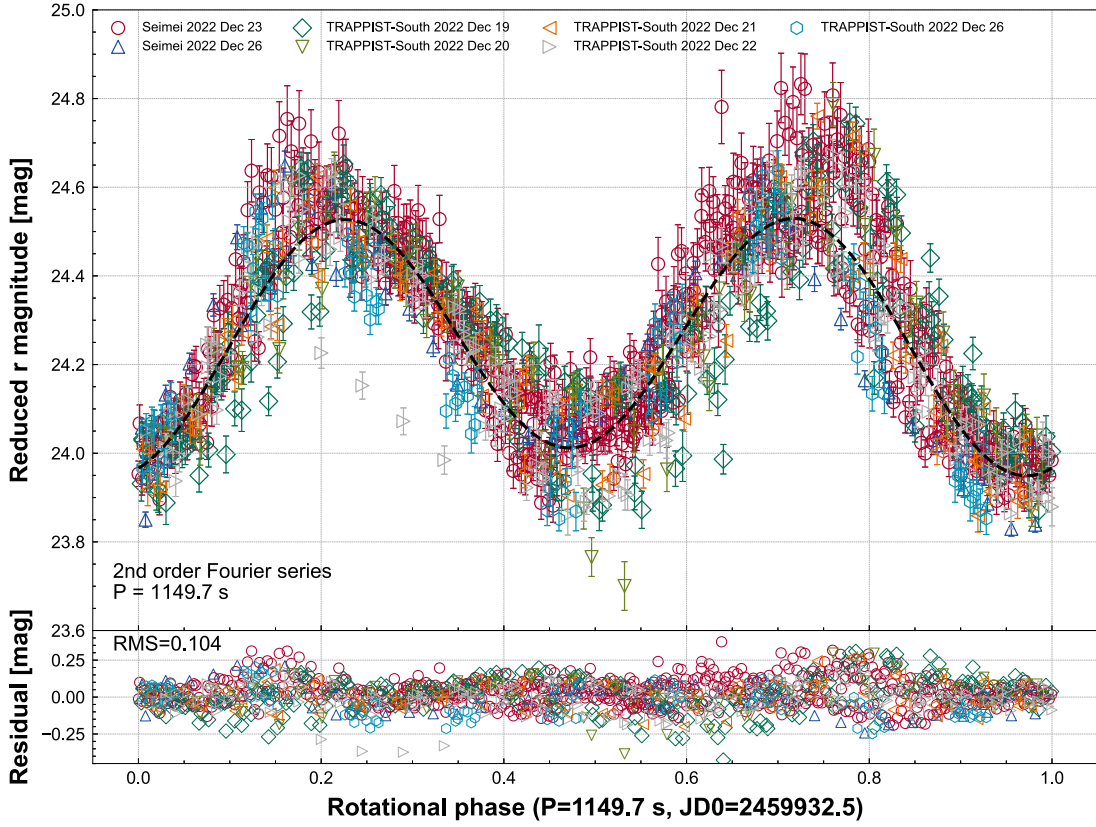
Figure 4. Phased lightcurves of 2015 RN$_{35}$. All lightcurves in reduced r magnitude are folded with a period of 1149.7 s. Phase zero is set to JD 2459932.5. Bars indicate the 1σ uncertainties of measurements. The model curve fitted to the lightcurves is shown by the dashed line.
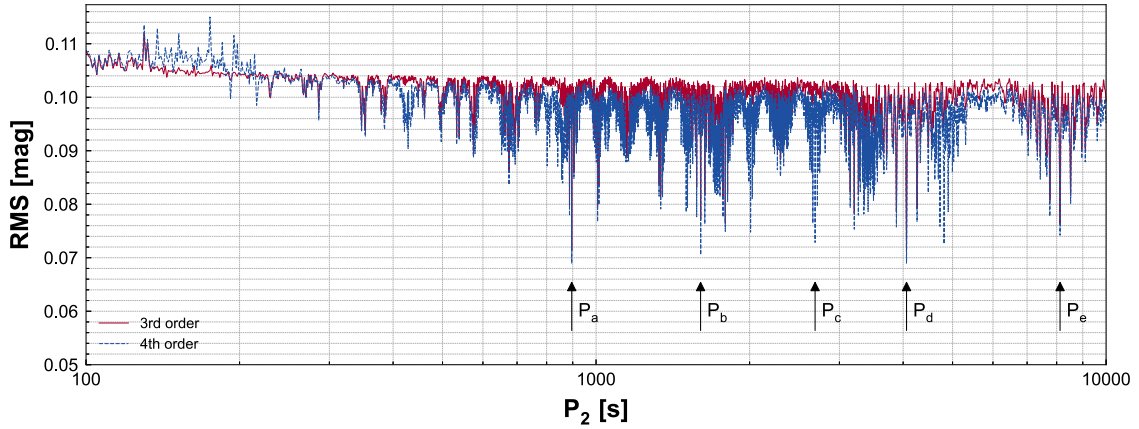

Figure 5. rms residuals between observed and model lightcurves of 2015 RN$_{35}$ fixing P_1 at 1149.7 s. Residuals using two-dimensional Fourier series with m of 3 and m of 4 are shown by solid and dashed lines, respectively. Five periods with smaller rms in either case are indicated.

We renormalize those spectra at 0.481 μm as follows:

$$R'(\lambda) = \frac{R(\lambda)}{R(0.481\ \mu m)}, \qquad (6)$$

where $R'(\lambda)$ is the renormalized reflectance at λ, $R(\lambda)$ is the original reflectance at wavelength λ, and $R(0.481\ \mu m)$ is the original reflectance at a wavelength of 0.481 μm.

3.3. Phase Curves

We observed 2015 RN$_{35}$ across a wide range of phase angles from 2° to 30°, which gives us a well-sampled phase curve as shown in Figure 9. We converted the g- and r-band magnitudes in the Pan-STARRS system to the V-band magnitude in the Johnson system using the equations in Tonry et al. (2012). We stacked 20 images obtained in 2023 January to make a decent detection of 2015 RN$_{35}$ for photometry as shown in the upper panels of Figure 1. The total integration time, 1200 s, is compatible with one of the characteristic periods of 2015 RN$_{35}$, P_1 of 1149.7 s. Thus, the effects of rotation have been corrected in the phase curves of 2015 RN$_{35}$.

We derived an absolute magnitude in the V band, H, and slope parameters, G_1 and G_2, with the H–G_1–G_2 model
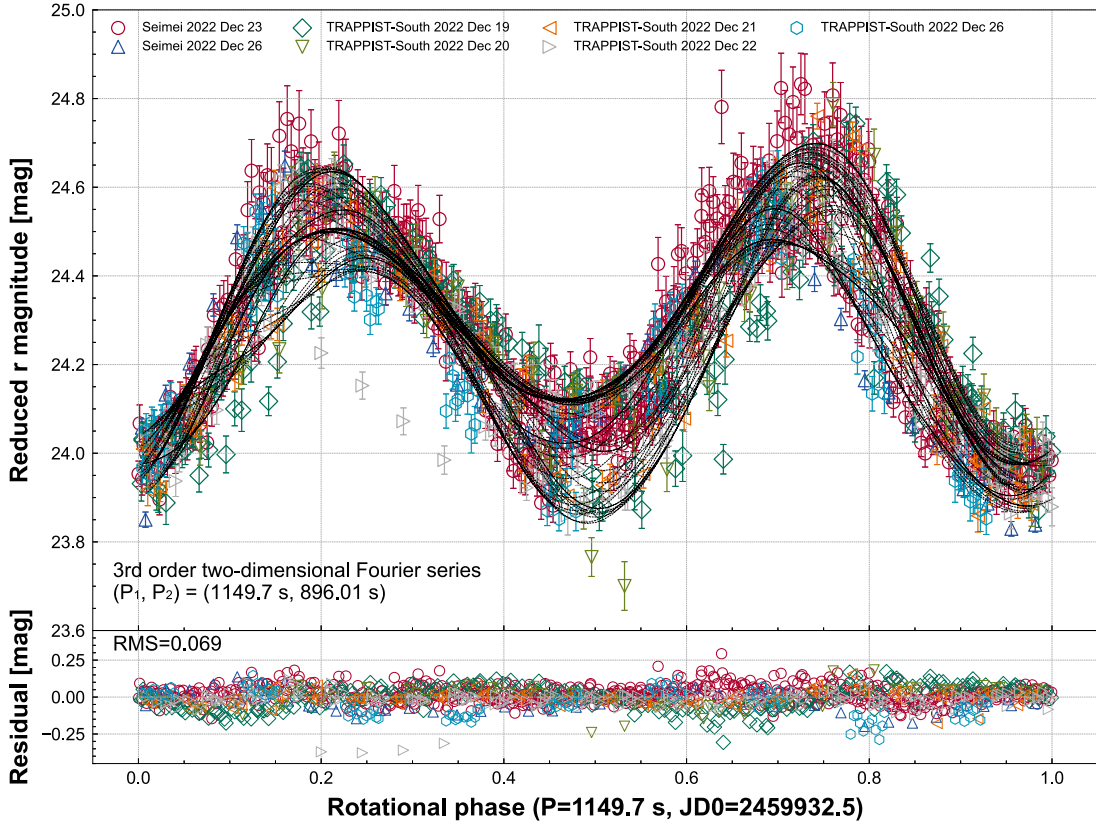
Figure 6. Phased lightcurves of 2015 RN$_{35}$ with two-dimensional Fourier series. All lightcurves in reduced r magnitude are folded with P_1 of 1149.7 s and P_2 of 896.01 s. Phase zero is set to JD 2459932.5. Bars indicate the 1σ uncertainties. Model curves fitted to lightcurves are shown by dashed lines.
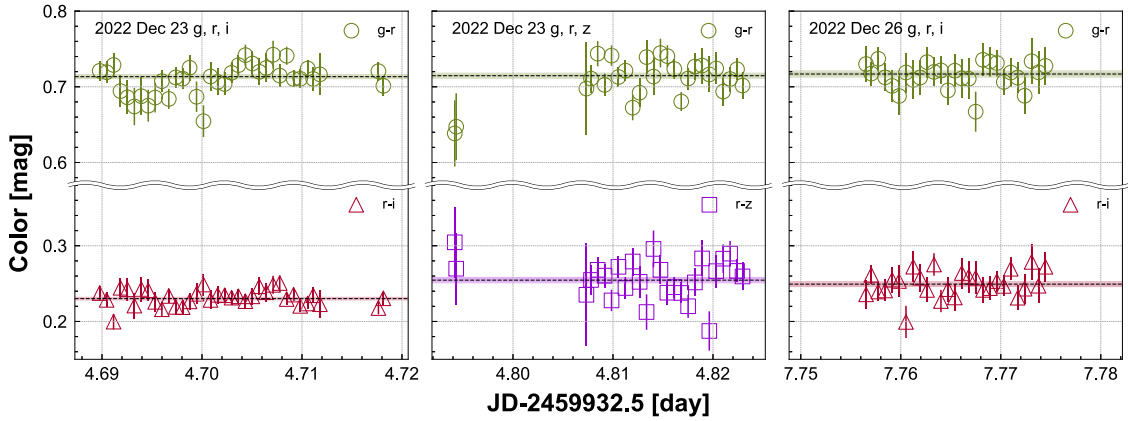
Figure 7. Time-series colors of 2015 RN$_{35}$. The $g - r$, $r - i$, and $i - z$ colors are shown by circles, triangles, and squares, respectively. Binning of 60 s is performed for all colors. Bars indicate the 1σ uncertainties. The weighted mean and its error are indicated by dashed lines and shaded areas, respectively.

(Muinonen et al. 2010):

$$V_{\mathrm{red}}(\alpha) = H - 2.5\log_{10}[G_1\Phi_1(\alpha) + G_2\Phi_2(\alpha) + (1 - G_1 - G_2)\Phi_3(\alpha)], \tag{7}$$

where $V_{\mathrm{red}}(\alpha)$ is a reduced magnitude in the V band at a phase angle of α. Φ_1, Φ_2, and Φ_3 are phase functions written as follows:

$$\Phi_1(\alpha) = 1 - \frac{6\alpha}{\pi}, \tag{8}$$

$$\Phi_2(\alpha) = 1 - \frac{9\alpha}{5\pi}, \tag{9}$$

$$\Phi_3(\alpha) = \exp\left(-4\pi \tan^{2/3}\frac{\alpha}{2}\right). \tag{10}$$

The uncertainties of H, G_1, and G_2 were estimated with the Monte Carlo technique. We made 1000 phase curves by randomly resampling the data assuming each observed datum follows a normal distribution whose standard deviation is a standard error of weighted mean magnitude. We derived H of 23.9 ± 0.2, G_1 of -0.10 ± 0.08, and G_2 of 0.8 ± 0.1. The
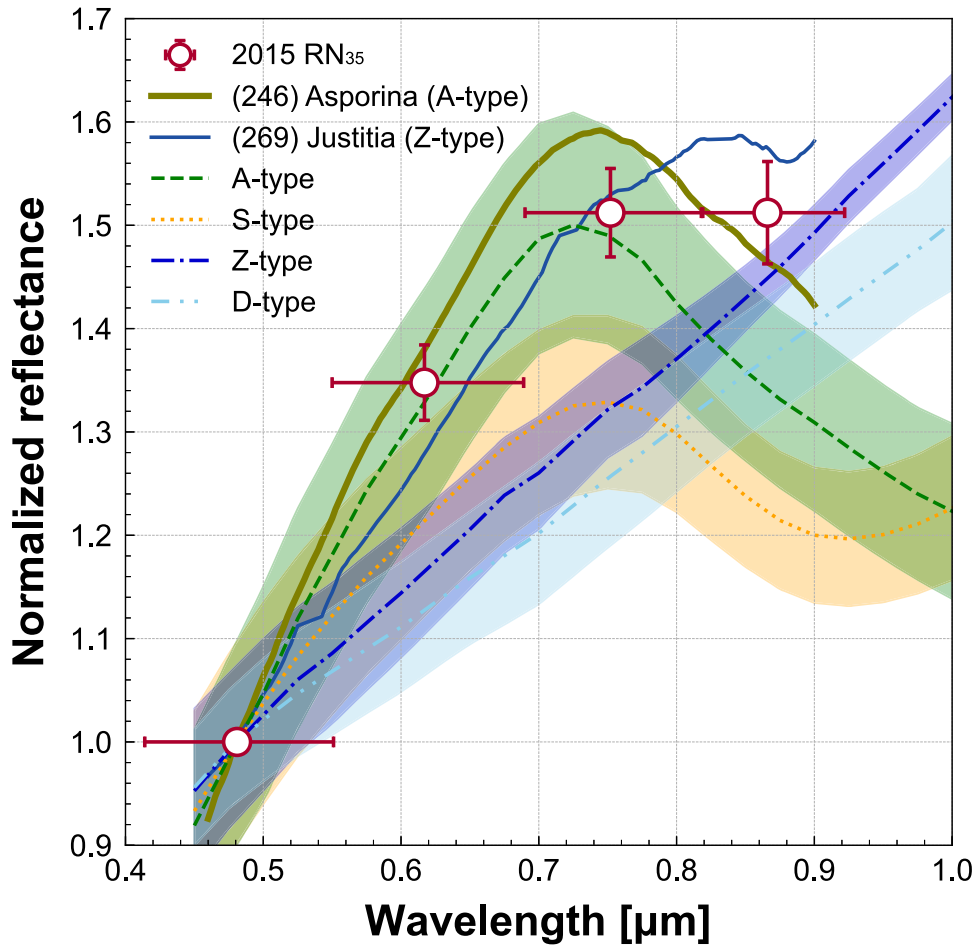
Figure 8. Reflectance spectrum of 2015 RN$_{35}$ (circles). Vertical bars indicate the 1σ uncertainties. Horizontal bars indicate the filter bandwidths. Template spectra of A-type (dashed line), S-type (dotted line), Z-type (dotted–dashed line), and D-type (double dotted–dashed line) are shown (Mahlke et al. 2022). Shaded areas indicate the standard deviations of the template spectra. Visible spectra of the A-type asteroid (246) Asporina (thick solid line) and the Z-type asteroid (269) Justitia (thin solid line) are shown. The reflectance spectra are normalized at 0.481 μm.

absolute magnitude and slope parameters in the *g*, *r*, and *i* bands are also derived in Figure 9 for convenience.

4. Discussion

4.1. Possible Classification of 2015 RN$_{35}$

The visible spectrum of 2015 RN$_{35}$ suggests that it is a very red object (VRO) in the near-Earth region. We compare the spectrum with the class templates from Mahlke et al. (2022) in Figure 8. We also show the spectra of the A-type MBA (246) Asporina and the VRO in the main belt (269) Justitia. These two spectra were obtained with SpeX (Rayner et al. 2003) on the NASA Infrared Telescope Facility (IRTF). We obtained the two spectra via the M4AST online tool (Modeling for Asteroids; Popescu et al. 2012). Justitia is known to have a very red slope like the trans-Neptunian objects (TNOs; Hasegawa et al. 2021), and is classified as Z-type in the latest Mahlke taxonomy (Mahlke et al. 2022). We note that the spectrum of Justitia seems to be out of the range of the Z-type template in the visible wavelengths in Figure 8. This is because Justitia is classified as Z-type in Mahlke et al. (2022) using both visible and near-infrared spectra. Thus, Justitia is a bit redder than the typical Z-types. The Z-types have featureless and much redder spectra than the D-types.

We evaluate the goodness of fit between the spectrum of 2015 RN$_{35}$ and templates using the following quantity:

$$\delta^2 = \frac{1}{N}\sum_j (R_{\mathrm{obs},j} - R_{\mathrm{model},j})^2, \qquad (11)$$

where *N* is the number of reflectance values, $R_{\mathrm{obs},j}$ is the reflectance of 2015 RN$_{35}$ at wavelength *j*, and $R_{\mathrm{model},j}$ is the reflectance of a template spectrum at that wavelength. We found that the spectrum of 2015 RN$_{35}$ seems like those of A-types ($\delta^2 = 0.008$) and Z-types ($\delta^2 = 0.018$), whereas the spectrum does not fit well with S-types ($\delta^2 = 0.034$) and D-types ($\delta^2 = 0.033$). We note that having only visible colors is often not enough to determine the spectral types of asteroids. For instance, half of all objects classified as A-types based on spectra at visible wavelengths are not A-types in the near-infrared (DeMeo et al. 2019).

We classified 2015 RN$_{35}$ as an A- or Z-type in this study, where both types represent rare populations (Mahlke et al. 2022). A-type asteroids are olivine-rich asteroids and have similar spectra to those of the silicate mineral olivine and are thought to be a piece of differentiated planetesimal (DeMeo et al. 2019), while other studies propose that some A-types may originate from the mantle of Mars (Polishook et al. 2017). Thus, the A-types may have an important role in investigating

(a)

(b)
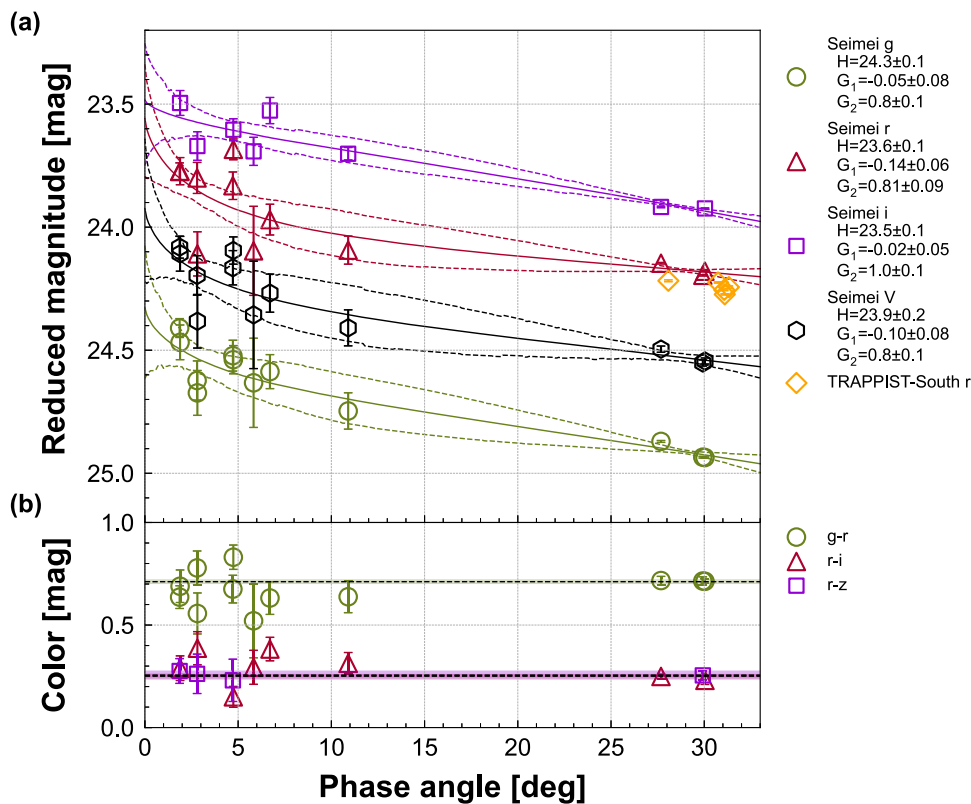
Figure 9. Phase-angle dependence of magnitude and colors of 2015 RN_{35}. (a) Mean reduced g-, r-, i-, z-, and V-band magnitudes (Seimei) are presented as circles, triangles, squares, diamonds, and hexagons, respectively. Mean reduced r-band magnitudes (TRAPPIST-South) are presented as diamonds. Bars indicate the 1σ uncertainties. The medians (50th percentile) of fitting model curves with the H–G_1–G_2 model are presented as solid lines. Uncertainty envelopes representing the 95% highest density interval values are shown by dashed lines. (b) Weighted mean $g - r$, $r - i$, and $r - z$ colors and their errors on each day are presented as circles, triangles, and squares, respectively. Bars indicate the 1σ uncertainties. Global weighted mean colors and their standard errors are indicated by dashed lines and shaded areas, respectively, although they are small and hard to see due to scale effects.
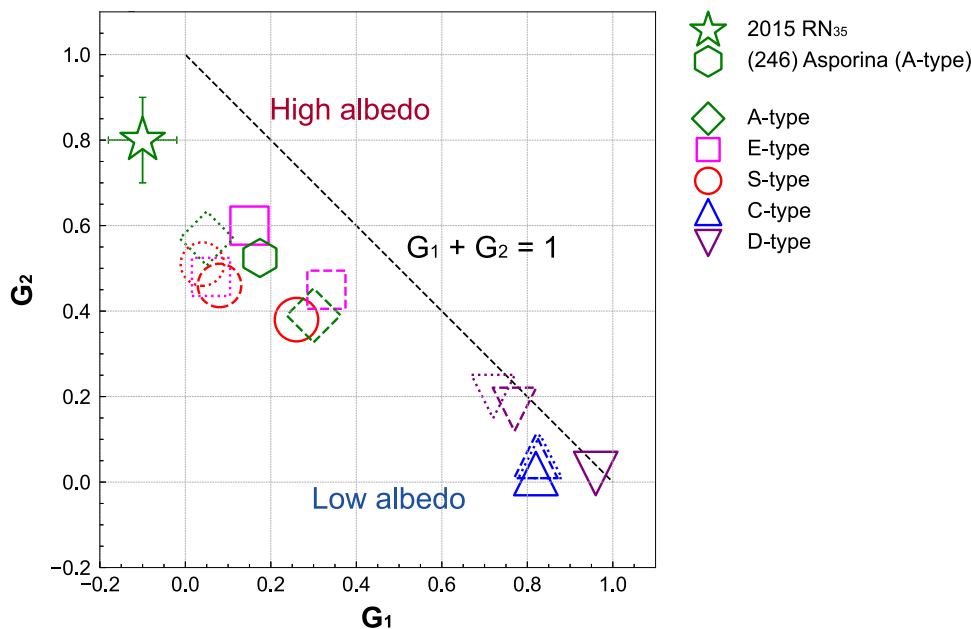
Figure 10. G_1 and G_2 of 2015 RN_{35} in the V band (star). Bars indicate the 1σ uncertainties. G_1 and G_2 of the A-type asteroid (246) Asporina are shown by the hexagon (Martikainen et al. 2021). Typical G_1 and G_2 values of A-, E-, S-, C-, and D-types are shown by diamonds, squares, circles, triangles, and inverted triangles, respectively. Markers are enclosed by solid lines (Shevchenko et al. 2016), dashed lines (cyan band; Mahlke et al. 2021), and dotted lines (orange band; Mahlke et al. 2021). The isochrone for $G_1 + G_2 = 1$ is plotted as the dashed line for convenience.

the formation of terrestrial planets. Recently, the two VROs, (203) Pompeja and (269) Justitia, were discovered in Hasegawa et al. (2021). Bourdelle de Micas et al. (2022) discovered the VRO (732) Tjilaki in the main belt. These VROs are classified as Z-types in the latest Mahlke taxonomy (Mahlke et al. 2022). In total, 23 asteroids including one NEA, (141670) 2002 JS_{100},

are classified as Z-type in Mahlke et al. (2022). The Z-types might have primitive organic materials on the surface like D-types (Barucci et al. 2018). Justitia is selected as the rendezvous target of the Emirates Mission to Explore the Asteroid Belt (Alhameli et al. 2023).

It is known that the slope parameters G_1 and G_2 have a tight correlation with the geometric albedo (Muinonen et al. 2010; Shevchenko et al. 2016). We show typical G_1 and G_2 values of A-, E-, S-, C- and D-types in Figure 10 (Shevchenko et al. 2016; Mahlke et al. 2021). We also plot G_1 and G_2 of the A-type MBA (246) Asporina derived using the sparse photometric observations from Gaia Data Release 2 (Martikainen et al. 2021). The smaller G_1 and larger G_2, by definition, mean that the slope of the phase curve is shallower. The slopes of high-albedo asteroids are shallower since the contribution of the shadow-hiding effect decreases as albedo increases (e.g., Belskaya & Shevchenko 2000), whereas those of low-albedo asteroids are steeper. Thus, the small G_1 and large G_2 of 2015 RN$_{35}$ are indicative of a high geometric albedo.

G_1 and G_2 of 2015 RN$_{35}$ seem a bit far from the typical values of A-types on Figure 10. But the typical values differ from each other by about 0.1–0.2 in the G_1–G_2 plane depending on the references. Thus, the discrepancy between the slope parameters of 2015 RN$_{35}$ and typical values does not necessarily indicate that 2015 RN$_{35}$ is an outlier. Therefore we concluded that 2015 RN$_{35}$ is an A-type asteroid in conjunction with the colors and slope parameters at visible wavelengths. We demonstrated that having photometry only at visible wavelengths is sufficient to determine the spectral type of asteroids, if it is across a wide range of phase angles.

Finally, we discuss other interpretations of the shallow phase slope of 2015 RN$_{35}$. Features such as self-gravity and rotation period are different for small and large asteroids. Small asteroids may have different surface properties to large asteroids. Terai et al. (2013) observed the tiny L-type NEA (367943) Duende (also known as 2012 DA$_{14}$) across a wide phase-angle range from 19° to 42°. They derived the slope parameter in the H–G model, G, as $0.44^{+0.06}_{-0.08}$, which is larger than the typical value of L-types. The tiny asteroid Duende has a shallow slope in the phase curve. They interpreted the large slope parameter or shallow slope as a difference in surface environment due to the lack of fine regolith or high geometric albedo. Small gravity on a tiny asteroid might lead to the lack of fine regolith on its surface. The shadow-hiding effect is weak when the fine regolith is deficient and the slope of the phase curve would be shallow. As for 2015 RN$_{35}$, in addition to the small gravity, the short rotation period of about 20 minutes also supports the hypothesis of the lack of fine regolith. Other recent studies showed that there is almost no correlation between albedo and slope parameters using the phase curves obtained in the framework of the IMPACTON project and the ATLAS survey (Rondón et al. 2019; Arcoverde et al. 2023). They interpreted that this is due to the difference in diameters of NEAs and MBAs. The trend is not clear since the number of samples is limited due to the observational difficulties. Comprehensive research on phase parameters is desired to reach a conclusion.

Various observations such as near-infrared spectroscopy and polarimetry are crucial in forthcoming approaches to studying 2015 RN$_{35}$ to conclusively determine its spectral type. The next two opportunities are in 2031 September and 2056 December,

where 2015 RN$_{35}$ will brighten to 21 and 16 mag in the V band, respectively.

4.2. Diameter Estimation of Tiny Asteroids

Estimation of asteroid sizes is important not only to evaluate a risk of impact to the Earth but also to plan exploration missions. However, small NEAs are often observed only at a few apparitions at relatively large phase angles compared to MBAs and TNOs. Thus, the absolute magnitude of the asteroid is often not well constrained. The absolute magnitude could be uncertain by ∼0.3 depending on whether the opposition surge exists (see, e.g., Belskaya et al. 2003). Jurić et al. (2002) and Pravec et al. (2012) independently estimated that there is a systematic uncertainty of H of about 0.4. In addition to the uncertainty of H, the geometric albedo is not well estimated for small bodies since observing opportunities are limited to only a short period, as in this study.

We estimated the absolute magnitude of 2015 RN$_{35}$ with high accuracy as 23.9 ± 0.2 through observations across a wide range of phase angles down to 2°. The surface colors as well as the slope of the phase curve indicate that 2015 RN$_{35}$ is a very red asteroid, probably classified as an A-type asteroid. The typical geometric albedo of A-types is estimated as 0.282 ± 0.101 and 0.28 ± 0.09 in Usui et al. (2013) and DeMeo et al. (2019), respectively. We assume the geometric albedo of 2015 RN$_{35}$ to be p_V of 0.28 ± 0.10. The diameter of an asteroid can be estimated with H and p_V using the following equation (Fowler & Chillemi 1992; Pravec & Harris 2007):

$$D = \frac{1329}{\sqrt{p_V}} \times 10^{-H/5}. \tag{12}$$

The diameter of 2015 RN$_{35}$ is estimated to be 41 ± 8 m. We updated the absolute magnitude of 2015 RN$_{35}$ by about 0.7 compared to H of 23.24 in JPL SBDB. Our study demonstrated that it is crucial to observe the asteroid in multiple bands at multiple epochs including where the phase angles are low in order to derive H and D accurately. Observations at very low phase angles are not possible for all NEAs. Detailed planning of observations is crucial for estimating the diameter of tiny asteroids.

4.3. Mission Accessibility

One of the important parameters in planning a spacecraft mission is Δv, which is the impulse required per unit of spacecraft mass to change the status of the spacecraft. We refer to the total Δv [18] as the sum of (i) the maneuver required to depart a circular Earth parking orbit at a notional 400 km altitude, (ii) the Δv required to match the NEA's velocity at arrival, (iii) the Δv required to depart the NEA, and (iv) the Δv (if any) required to control atmospheric entry speed on return to Earth. We queried the Δv of NEAs for the Near-Earth Object Human Space Flight Accessible Targets Study (NHATS; Abell et al. 2012).[19] The Δv of 2015 RN$_{35}$ is estimated as 11.801 km s^{-1} in the launch window between 2030 and 2035, which is smaller than the limit of NHATS, 12 km s^{-1}. In terms of the engineering aspect, 2015 RN$_{35}$ is a good candidate for a future spacecraft mission. From a scientific

---

[18] https://cneos.jpl.nasa.gov/nhats/
[19] https://ssd-api.jpl.nasa.gov/doc/nhats.html, last accessed 2023 August 10

point of view, 2015 RN$_{35}$, whether it is an A- or a Z-type NEA, is a great candidate for a future mission. Specifically, there are no planned future spacecraft missions to A-type asteroids.

5. Conclusions

We conducted multicolor photometry of the tiny NEA 2015 RN$_{35}$ over 17 nights in 2022 December and 2023 January. We observed 2015 RN$_{35}$ across a wide range of phase angles from $2°$ to $30°$ in the g, r, i, and z bands in the Pan-STARRS system. We found that 2015 RN$_{35}$ is in a nonprincipal axis spin state with two characteristic periods of 1149.7 ± 0.3 s and 896.01 ± 0.01 s. The visible spectrum of 2015 RN$_{35}$ is as red as (269) Justitia, one of the VROs in the main belt, which indicates that 2015 RN$_{35}$ can be classified as an A- or Z-type asteroid. Together with the shallow slope of the phase curve, we suppose 2015 RN$_{35}$ is a high-albedo A-type asteroid.

Various observations such as near-infrared spectroscopy and polarimetry are encouraged during the forthcoming approaches of 2015 RN$_{35}$. The next opportunity is in 2031 September, where 2015 RN$_{35}$ will brighten to 21 mag. Though additional follow-up observations are required to reach a conclusion, 2015 RN$_{35}$ is a possible mission-accessible A-type NEA with small Δv of 11.801 km s^{-1} in a launch window between 2030 and 2035.

ORCID iDs

Jin Beniyama ⓘ https://orcid.org/0000-0003-4863-5577
Ryou Ohsawa ⓘ https://orcid.org/0000-0001-5797-6010
Chrysa Avdellidou ⓘ https://orcid.org/0000-0001-8228-8789
Shigeyuki Sako ⓘ https://orcid.org/0000-0002-8792-2205
Masateru Ishiguro ⓘ https://orcid.org/0000-0002-7332-2479
Tomohiko Sekiguchi ⓘ https://orcid.org/0000-0003-1726-6158
Fumihiko Usui ⓘ https://orcid.org/0000-0003-2273-0103
Shinichi W. Kinoshita ⓘ https://orcid.org/0000-0001-5456-4977
Kianhong Lee ⓘ https://orcid.org/0000-0003-4814-0101
Marin Ferrais ⓘ https://orcid.org/0000-0002-0535-652X
Emmanuël Jehin ⓘ https://orcid.org/0000-0001-8923-488X

References

Abell, P. A., Barbee, B. W., Mink, R. G., et al. 2012, 43rd Annual LPSC, 2842
Alhameli, F. S., Parker, J. S., Caudill, M. T., et al. 2023, in Asteroids, Comets, and Meteors: ACM 2023 (Houston, TX: LPI), 2344
Arcoverde, P., Rondón, E., Monteiro, F., et al. 2023, MNRAS, 523, 739
Astropy Collaboration, Price-Whelan, A. M., & Sipőcz, B. M. 2018, AJ, 156, 123
Astropy Collaboration, Robitaille, T. P., Tollerud, E. J., et al. 2013, A&A, 558, A33
Avdellidou, C., Di Donna, A., Schultz, C., et al. 2020, Icar, 341, 113648
Barbary, K., Boone, K., Craig, M., Deil, C., & Rose, B. 2017, Kbarbary/Sep: V1.0.2, v1.0.2, Zenodo, doi:10.5281/zenodo.896928
Barucci, M. A., Perna, D., Popescu, M., et al. 2018, MNRAS, 476, 4481
Belskaya, I. N., & Shevchenko, V. G. 2000, Icar, 147, 94
Belskaya, I. N., Shevchenko, V. G., Kiselev, N. N., et al. 2003, Icar, 166, 276
Beniyama, J., Sako, S., Ohsawa, R., et al. 2022, PASJ, 74, 877
Beniyama, J., Sako, S., Ohtsuka, K., et al. 2023a, ApJ, 955, 143

Beniyama, J., Sekiguchi, T., Kuroda, D., et al. 2023b, PASJ, 75, 297
Bertin, E., & Arnouts, S. 1996, A&AS, 117, 393
Borisov, G., Christou, A. A., Colas, F., et al. 2018, A&A, 618, A178
Bourdelle de Micas, J., Fornasier, S., Avdellidou, C., et al. 2022, A&A, 665, A83
Bowell, E., Hapke, B., Domingue, D., et al. 1989, in Asteroids II, ed. R. P. Binzel, T. Gehrels, & M. S. Matthews (Tucson, AZ: Univ. Arizona Press), 524
Cambioni, S., Delbo, M., Poggiali, G., et al. 2021, Natur, 598, 49
Chambers, K. C., Magnier, E. A., Metcalfe, N., et al. 2016, arXiv:1612.05560
Colazo, M., Fornari, C., Ciancia, G., et al. 2023, MPBu, 50, 235
Delbo, M., Fornari, C., Ciancia, G., et al. 2017, Sci, 357, 1026
DeMeo, F. E., Polishook, D., Carry, B., et al. 2019, Icar, 322, 13
Fenucci, M., Novaković, B., & Marčeta, D. 2023, A&A, 675, A134
Fenucci, M., Novaković, B., Vokrouhlický, D., & Weryk, R. J. 2021, A&A, 647, A61
Fowler, J. W., & Chillemi, J. R. 1992, Technical Report 2049, Philips Lab
Franco, L., Marchini, A., Iozzi, M., et al. 2023, MPBu, 50, 173
Ginsburg, A., Sipőcz, B. M., Brasseur, C. E., et al. 2019, AJ, 157, 98
Harris, A. W., & Lupishko, D. F. 1989, in Asteroids II, ed. R. P. Binzel, T. Gehrels, & M. S. Matthews (Tucson, AZ: Univ. Arizona Press), 39
Harris, C. R., Millman, K. J., van der Walt, S. J., et al. 2020, Natur, 585, 357
Hasegawa, S., Marsset, M., DeMeo, F. E., et al. 2021, ApJL, 916, L6
Hunter, J. D. 2007, CSE, 9, 90
Ieva, S., Arcoverde, P., Rondón, E., et al. 2022, MNRAS, 513, 3104
Jehin, E., Gillon, M., Queloz, D., et al. 2011, Msngr, 145, 2
Jurić, M., Ivezić, Ž., & Lupton, R. H. 2002, AJ, 124, 1776
Koleńczuk, P., Kwiatkowski, T., Kamińska, M., & Kaminski, K. 2023, in Asteroids, Comets, and Meteors: ACM 2023 (Houston, TX: LPI), 2398
Kurita, M., Kino, M., Iwamuro, F., et al. 2020, PASJ, 72, 48
Lang, D., Hogg, D. W., Mierle, K., Blanton, M., & Roweis, S. 2010, AJ, 139, 1782
Lee, H. J., Kim, M. J., Marciniak, A., et al. 2022, A&A, 661, L3
Lee, H.-J., Moon, H.-K., Kim, M.-J., et al. 2017, JKAS, 50, 41
Licandro, J., Popescu, M., Tatsumi, E., et al. 2023, MNRAS, 521, 3784
Lomb, N. R. 1976, Ap&SS, 39, 447
Mahlke, M., Carry, B., & Denneau, L. 2021, Icar, 354, 114094
Mahlke, M., Carry, B., & Mattei, P. A. 2022, A&A, 665, A26
Martikainen, J., Muinonen, K., Penttilä, A., Cellino, A., & Wang, X. B. 2021, A&A, 649, A98
McCully, C., Crawford, S., Kovacs, G., et al. 2018, Astropy/Astroscrappy: V1.0.5 Zenodo Release, v1.0.5, Zenodo, doi:10.5281/zenodo.1482019
Mommert, M. 2017, A&C, 18, 47
Mommert, M., Farnocchia, D., Hora, J. L., et al. 2014a, ApJL, 789, L22
Mommert, M., Hora, J. L., Farnocchia, D., et al. 2014b, ApJ, 786, 148
Muinonen, K., Belskaya, I. N., Cellino, A., et al. 2010, Icar, 209, 542
Oliphant, T. E. 2015, Guide to NumPy (2nd edn.; North Charleston, SC: CreateSpace Independent Publishing Platform)
Petrov, N. A., Vasil'ev, A. A., Kuteeva, G. A., & Sokolov, L. L. 2018, SoSyR, 52, 326
Polishook, D., Jacobson, S. A., Morbidelli, A., & Aharonson, O. 2017, NatAs, 1, 0179
Popescu, M., Birlan, M., & Nedelcu, D. A. 2012, A&A, 544, A130
Pravec, P., & Harris, A. W. 2007, Icar, 190, 250
Pravec, P., Harris, A. W., Kušnirák, P., Galád, A., & Hornoch, K. 2012, Icar, 221, 365
Pravec, P., Harris, A. W., Scheirich, P., et al. 2005, Icar, 173, 108
Pravec, P., Scheirich, P., Ďurech, J., et al. 2014, Icar, 233, 48
Rayner, J. T., Toomey, D. W., Onaka, P. M., et al. 2003, PASP, 115, 362
Reback, J., jbrockmendel, McKinney, W., et al. 2021, pandas-dev/pandas: Pandas 1.3.4, v1.3.4, Zenodo, doi:10.5281/zenodo.5574486
Reddy, V., Gary, B. L., Sanchez, J. A., et al. 2015, ApJ, 811, 65
Reddy, V., Sanchez, J. A., Bottke, W. F., et al. 2016, AJ, 152, 162
Rondón, E., Arcoverde, P., Monteiro, F., et al. 2019, MNRAS, 484, 2499
Rondón, E., Lazzaro, D., Carvano, J., et al. 2022, Icar, 372, 114723
Rubincam, D. P. 2000, Icar, 148, 2
Scargle, J. D. 1982, ApJ, 263, 835
Shevchenko, V. G., Belskaya, I. N., Muinonen, K., et al. 2016, P&SS, 123, 101
Terai, T., Urakawa, S., Takahashi, J., et al. 2013, A&A, 559, A106
Thirouin, A., Moskovitz, N., Binzel, R. P., et al. 2016, AJ, 152, 163
Thirouin, A., Moskovitz, N. A., Binzel, R. P., et al. 2018, ApJS, 239, 4
Tonry, J. L., Stubbs, C. W., Lykke, K. R., et al. 2012, ApJ, 750, 99
Usui, F., Kasuga, T., Hasegawa, S., et al. 2013, ApJ, 762, 56
van Dokkum, P. G. 2001, PASP, 113, 1420
VanderPlas, J. T. 2018, ApJS, 236, 16
Virtanen, P., Gommers, R., Oliphant, T. E., et al. 2020, NatMe, 17, 261
Vokrouhlický, D. 1998, A&A, 335, 1093
Willmer, C. N. A. 2018, ApJS, 236, 47